

## Article

# Study of Wind Field and Surface Wind Pressure of Solar Greenhouse Group under Valley Topography Conditions

Zixuan Gao, Jing Xu , Rui Wang, Yi Jiang and Zongmin Liang \*

College of Water Resources and Civil Engineering, China Agricultural University, Beijing 100083, China; renaissance6688@gmail.com (Z.G.); xujing@cau.edu.cn (J.X.); sy20223092031@cau.edu.cn (R.W.); youandme419@163.com (Y.J.)

\* Correspondence: liangzm@cau.edu.cn

**Abstract:** There is a wind interference effect between greenhouses in a group arrangement of solar greenhouse groups. To ensure the structural integrity of greenhouse groups situated in valleys, it becomes imperative to analyze both the wind pressure distribution patterns and the wind interference effects. This arises from the recognition that the wind load coefficients applicable to solar greenhouse groups nestled within valleys deviate from those observed in flat plains. The application of the contour modeling method facilitated a realistic reconstruction of the authentic topography within the study area. Subsequently, a wind field simulation was executed specifically for the constructed valley. The resultant wind field data for the studied valley area were then obtained. In the valley, nine solar greenhouses were systematically arranged in a three by three configuration. Special attention was directed towards assessing the surface wind pressures derived meticulously from the simulated wind field and wind direction angle of  $0^\circ$ . The findings elucidate the following: (a) The wind speed ratio exhibits a diminution on the leeward side of the mountain as compared to the windward side, with a notably reduced wind speed ratio observed in proximity to the mountain. (b) An amplification effect is discernible in the peripheral zone adjacent to the leading row of greenhouses, proximate to the incoming airflow. Particular emphasis is warranted regarding the reversal of wind direction observed in the secondary row of greenhouses positioned along the north wall and front roof, specifically at a wind angle of  $0^\circ$ , owing to the pronounced influence of interference effects. Hence, when undertaking the design and construction of a cluster of solar greenhouses within the valley terrain of Tibet, meticulous consideration must be directed towards both the meticulous calculation of wind loads within the periphery of the greenhouses and the judicious selection of the grouping's location.

**Keywords:** valley topography; numerical simulation; solar greenhouse group; wind pressure coefficient



**Citation:** Gao, Z.; Xu, J.; Wang, R.; Jiang, Y.; Liang, Z. Study of Wind Field and Surface Wind Pressure of Solar Greenhouse Group under Valley Topography Conditions. *Agronomy* **2024**, *14*, 973. <https://doi.org/10.3390/agronomy14050973>

Academic Editor: Pedro Javier Zapata

Received: 7 April 2024

Revised: 24 April 2024

Accepted: 30 April 2024

Published: 6 May 2024



**Copyright:** © 2024 by the authors. Licensee MDPI, Basel, Switzerland. This article is an open access article distributed under the terms and conditions of the Creative Commons Attribution (CC BY) license (<https://creativecommons.org/licenses/by/4.0/>).

## 1. Introduction

The unique environmental conditions of Tibet, characterized by high altitude and correspondingly low soil and air temperatures, pose significant challenges for conventional agricultural practices, particularly in the cultivation of warm-weather vegetables. As such, the adoption of facility horticulture emerges as an imperative strategy to address the pressing need for reliable vegetable supply to the indigenous population. Simultaneously, Tibet occupies a low-latitude zone characterized by prolonged sunshine hours and abundant solar energy reservoirs, thus providing an optimal environment for the advancement of facility horticulture endeavors. In the past decade, there has been a remarkable surge in the expansion of greenhouse vegetable cultivation across Tibet [1].

The solar greenhouse framework is distinguished by its lightweight construction; expansive span; and elongated, slender poles, collectively constituting a flexible structural paradigm. Furthermore, the roofing materials employed in solar greenhouses are characterized by their lightweight nature and susceptibility to wind dynamics [2,3]. Incidents of high winds causing damage to solar greenhouse roofs and their supporting structures

have intermittently occurred, leading to substantial economic losses and disruptions in normal production. Furthermore, such occurrences pose significant risks to the safety of personnel, underscoring the urgent need for enhanced structural resilience measures [4–6]. Addressing these vulnerabilities is imperative to mitigate economic impact and ensure the safety and continuity of operations within solar greenhouse facilities.

The distribution of solar greenhouses in Tibet predominantly spans narrower valley regions, characterized by intricate topographical features and geomorphological complexities. Consequently, the wind field in the valleys exhibits pronounced variations and inhomogeneities in wind speed, direction, turbulence structure, and wind pressure [7–9]. Winds affected by environmental interference impose complex and adverse wind loads upon solar greenhouse structures, necessitating thorough investigation and analysis. To elucidate the characteristics of the wind load action of the solar greenhouse situated within valley regions, it is essential to commence by acquiring data pertaining to the wind field characteristics within the specific valley locality.

The most accurate way to obtain information about the actual wind field is to collect field measurements. However, the promotion of this approach faces impediments in complex terrain areas, attributable to constraints related to climate, topography, available manpower, and material resources [10]. Commonly, numerical simulation techniques are deployed as alternative methods. Relative to wind tunnel testing and field measurements, the numerical simulation approach excels at capturing wind information across the entirety of space under full-scale conditions, obviating the need to account for scaling effects. This constitutes a discernible advantage in the analysis of wind fields, particularly in complex terrains. The numerical simulations encompass two primary categories: computational fluid dynamics (CFD)-based simulations and mesoscale numerical models are exemplified by weather research and forecasting (WRF). Numerous studies [11–14] have employed the WRF model to replicate near-surface wind patterns in intricate terrains, but the mesoscale model encounters challenges when simulating wind dynamics within steep canyons, exhibiting limitations and susceptibility to integral overflow in mountainous regions [15].

A numerical simulation methodology using CFD has emerged as the predominant research tool for investigating wind dynamics. To examine the airflow dynamics over an unconventional converging channel topography, characterized by a deep valley upstream and a flat plain downstream, Song et al. [16] conducted CFD simulations employing the standard  $k$ - $\epsilon$  model. Their investigation aimed to elucidate alterations in the downwind structure under predominant inlet wind conditions. Wang et al. [17] used Fluent 14.0 software to simulate wind fields with varying mountain slopes, morphology, and patterns. Zhuo et al. [18] used computational fluid dynamic numerical simulation to study the wind profiles at the mid-span point of the main girder in the ideal canyon and the real canyon model under varied degrees of roughness. Yang et al. [19] conducted large-eddy simulations to investigate the effects of wind shear coefficients and upstream turbulence intensities on the complex wind flow fields over simplified 3D hills. The construction of buildings in intricate terrain requires not only a careful study of the distribution of wind fields in such environments but also an analysis of the wind pressures on the surfaces of the buildings as well as the intricate interactions between neighboring buildings in the built environment.

Numerous scholars have studied the surface wind pressure and disturbance effects of building groups. Chen et al. [20] discovered that aligning air-supported membrane structures parallel to downstream counterparts significantly amplifies the wind load, particularly under oblique wind conditions. This configuration resulted in a remarkable 65% increase in the average wind load within the most vulnerable area. Pal et al. [21] examined the comparative wind-induced mutual interference effects between two-sided square and fish-shaped planar building models of equal volume. Sharma et al. [22] investigated the impact of interference effects on the cylindrical roofs of low-rise buildings by manipulating both the roof pitch and the incident wind angle. Wu et al. [23] investigated the wind pressure coefficients and shape factors of the wind load on the surface of a group of five

rows and six columns of greenhouses with varying incoming currents and spacing using the realizable  $k-\epsilon$  model.

The above literature illustrates the applicability of CFD in the study of wind fields in complex terrain with wind pressures on the surfaces of low-rise buildings. In this study, the CFD method is employed to initially simulate the wind laws within the valley region, where a group of solar greenhouses is situated in the eastern periphery of Lhasa city. Subsequently, the wind field characteristics prevalent within the valley are analyzed, followed by wind load simulations specific to the solar greenhouse group nestled within the valley. And, the surface wind pressure distribution of the solar greenhouse ensemble was systematically analyzed, culminating in the determination of surface wind pressure coefficients and the shape factors of the wind load for each individual solar greenhouse. The outcomes of these investigations offer valuable insights for informing the optimal siting of solar greenhouses within the Tibetan valley and for precision calculations of the surface wind load associated with each greenhouse within the group.

## 2. Model Dimensions and Model Establishment

### 2.1. Valley Topography Construction

The research focus of this study pertains to a solar greenhouse group situated within the eastern region of Lhasa city. The site is the valley of the Lhasa River, focusing on the wind field and its wind loading on the solar greenhouse group (the locations are shown in yellow in Figures 1 and 2) within the valley. Particularly, within the Lhasa city area (as shown in the red box in Figure 2), diurnal wind patterns predominantly feature easterly winds, followed by southeasterly counterparts [24]. Given the architectural attributes of solar greenhouses as low-profile constructions, this investigation specifically delves into the analysis of ground-level axial winds aligned with the southeast direction along the valley, thereby highlighting their potential influence on the solar greenhouse.

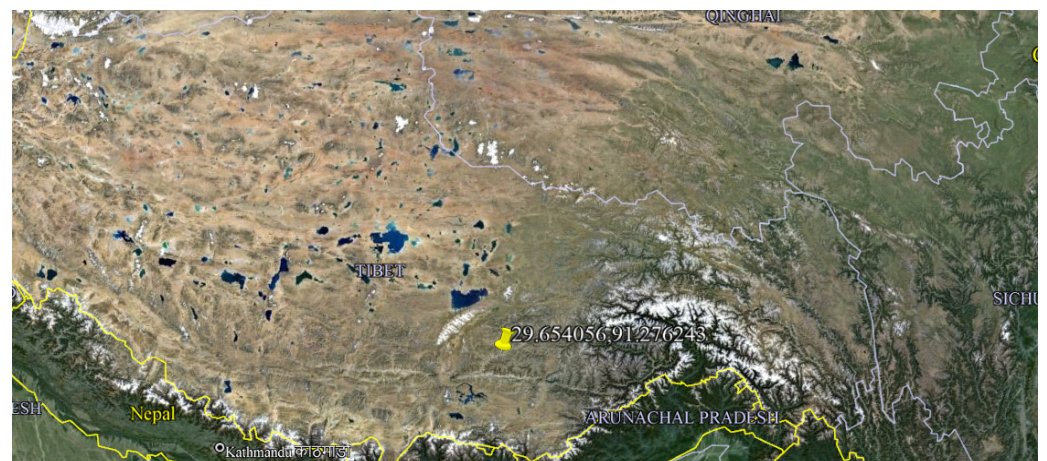


**Figure 1.** Location of the greenhouse groups in Tibet.

In the examination of wind field characteristics amidst complex terrains, the determination of the inflow condition stands out as a notably challenging endeavor. A requisite in this investigative pursuit lies in the judicious establishment of a reasoned and precise inflow condition [25]. The prevailing approach to discerning inlet conditions for numerical simulations of wind fields within complex terrains is presently dominated by the Fitted empirical profile method. However, the direct application of the method makes it difficult to reconcile the preservation of real terrain features with real inflow conditions. Li et al. [25] introduced the interpolated multiscale profile, delineating a novel paradigm by partitioning computational domains into distinct upstream and downstream segments. This deliberate separation facilitates the extraction of velocity and turbulence characteristics from the outlet of the upstream computational domain. These extracted parameters serve as precise inlet boundary conditions for the ensuing flow field within the downstream computational

domain. This innovative methodology underscores a strategic approach to seamlessly transferring information across domains, enhancing the fidelity of downstream simulations. This innovative approach, as advanced by Li et al. [25], not only upholds the intricate geomorphological attributes inherent in the original complex terrain wind field but also refines the imposition of inlet boundary conditions with heightened precision. Simultaneously, it circumvents the challenges associated with the conventional methodology, which entails extensive computational resource consumption. Unlike the traditional practice of selecting expansive terrain areas to generate a myriad of computational domain grids, this method enhances the efficiency and accuracy of numerical simulations in complex terrains, thereby representing a notable stride towards expeditious and refined computational analyses.



**Figure 2.** Schematic diagram of Lhasa urban area, location of solar greenhouse groups, and incoming wind direction.

The solar greenhouse group under study is located in the intricate topography of the Lhasa River Valley. In order to accurately simulate the wind field in this unique terrain, the IMP method was chosen as the analysis method in this study. Two spatial domains, each spanning 5 km by 5 km, were delineated to capture the intricate topographical features of the valley. Designated as region A (upstream) and region B (downstream), their spatial configuration is illustrated in Figure 3. The altitude of region A is from 3643 m to 4341 m and the altitude of region B is from 3628 m to 4043 m; the solar greenhouse group is located in region B.



**Figure 3.** Topography selected using the interpolated multiscale profile method.

Following the delineation of the study area, the imperative next step involves the construction of a 3D model tailored for CFD simulation. This modeling procedure conventionally relies on the application of contour-based methodologies [26], as shown in Figure 4.

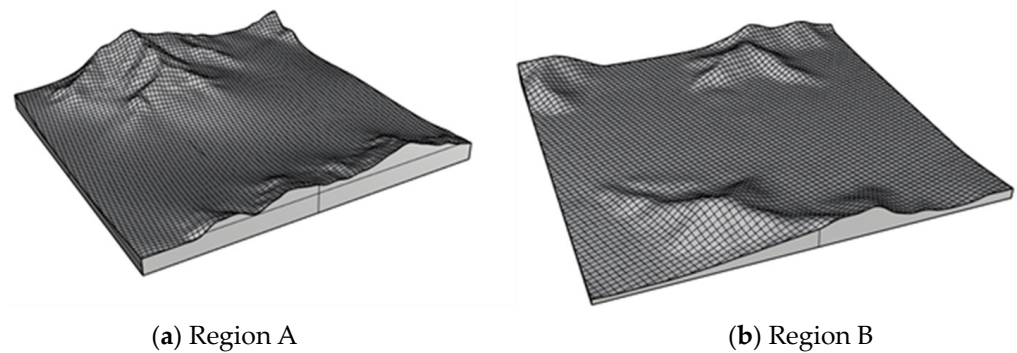


**Figure 4.** Three-dimensional topographic model.

### 2.2. Construction of Greenhouse Groups

As shown in Figure 5, the greenhouse boasts an impressive east–west length of 60 m, a north–south width measuring  $B_2 = 12.6$  m, a rear wall standing at a height of  $H_1 = 3.5$  m, a ridge soaring to  $H_2 = 5.5$  m, and a rear roof with a horizontal projection width of  $B_1 = 1.6$  m.

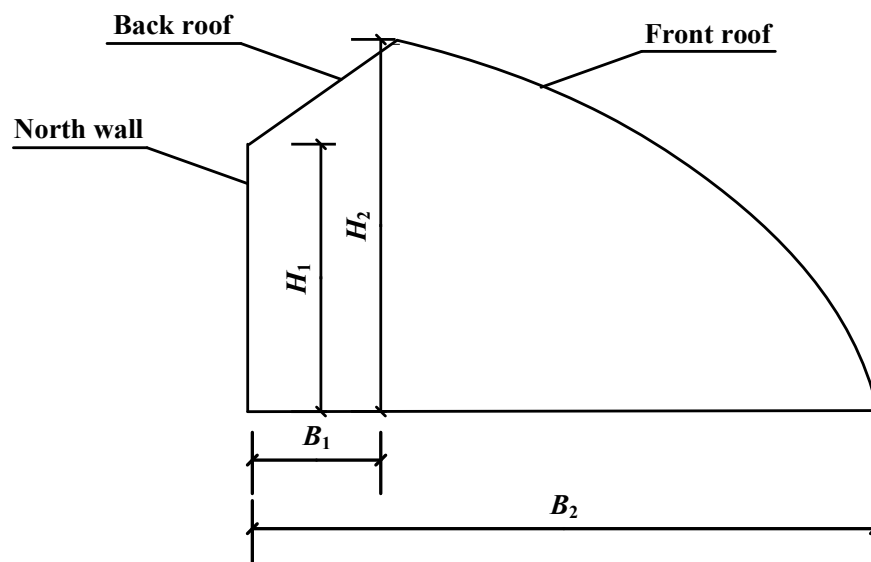


**Figure 5.** Surface profile of solar greenhouse.

Figure 6 illustrates a group comprising three rows and three columns of solar greenhouses, the focal point of this investigation. In determining the spacing between these structures, factors such as light penetration, traffic flow, and land efficiency are carefully considered. Accordingly, a distance of 6 m is established between adjacent east–west solar greenhouses, while a distance of 9 m is maintained between those situated between north and south. In Figure 6,  $L_x$  is the total east–west length of the greenhouse group,  $L_{xn}$  is the east–west spacing of the greenhouses,  $D_z$  is the total north–south length of the solar greenhouse group, and  $D$  is the north–south spacing of the greenhouses. The solar greenhouses are systematically indexed based on their spatial orientation within the grid. Along the north–south axis, the rows are designated as 1, 2, and 3, while along the east–west axis, the columns are denoted as 1, 2, and 3. Consequently, the solar greenhouses are labeled using a dual numbering system, such as 1-1, 1-2, 1-3, 2-1, 2-2, 2-3, 3-1, 3-2, and 3-3, to denote their precise positions within the grid.

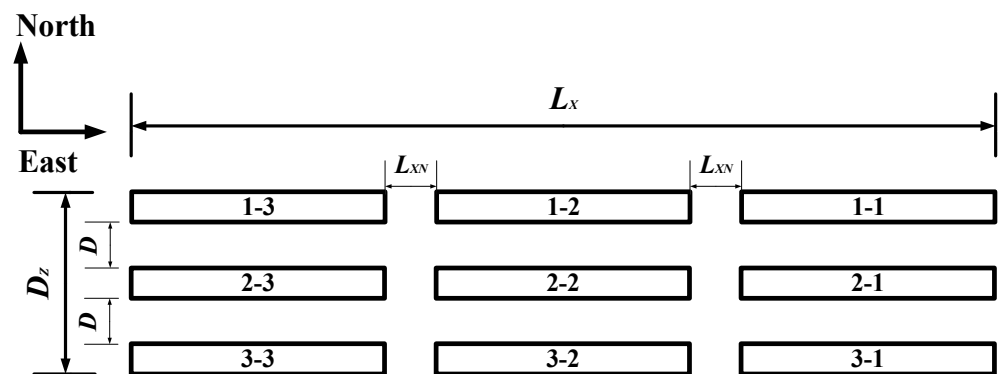


Figure 6. Greenhouse group's model.

### 2.3. Determination of Fluid Domain Height

A blockage rate below 3% in wind simulations can lead to excessively large fluid domains, significantly impeding simulation efficiency. Research by Li et al. [15] indicates that alterations in the fluid domain's dimensions—whether spanning 3000 or 6000 m—do not influence the wind field's structure below 600 m. For solar greenhouses, which are low-lying structures, the focus on the near-surface wind field in valleys suffices for assessment. Notably, region A exhibits an altitude difference nearing 700 m, while region B experiences an altitude difference of approximately 400 m. In both regions, the upper limits of the fluid domain are constrained to 3000 m, as shown in Figure 7.

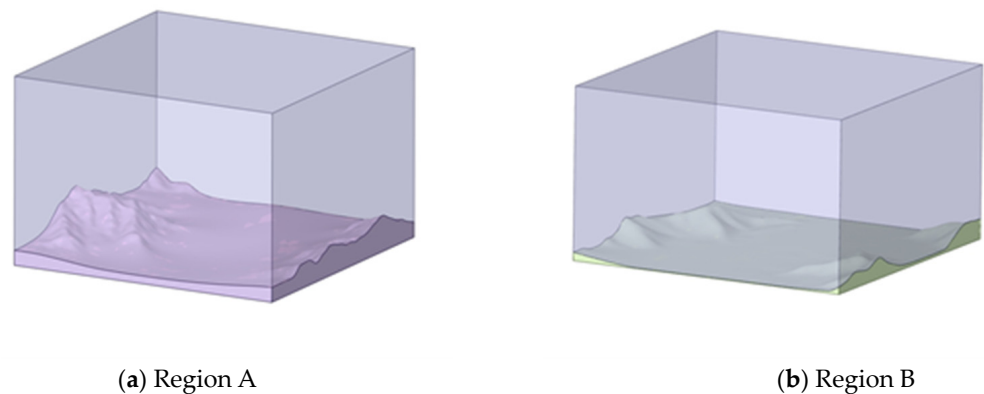


Figure 7. Valley fluid domain.

## 3. Results and Discussion of Wind Field

### 3.1. Surface Roughness

The distribution of wind fields within complex terrains is intricately influenced by two primary factors: the topographic and geomorphological characteristics at a macroscopic scale, alongside subsurface conditions operating at a microscopic level. Physical mountain models serve to depict surface topographic features, while ground roughness serves as an indicator delineating subsurface conditions.

The surface cover types identified through ArcGIS analysis are within simulation regions A and B. The predominant land cover categories observed in both areas comprise grasslands, agricultural fields, and bare land. Detailed breakdowns of the land cover distributions for these regions are presented in Table 1, providing insights into the respective extents of these identified cover types. The quantification of vegetation's aerodynamic roughness emerges from a mathematical operation involving the normalization of kinetic roughness multiplied by the canopy height. The quantification of normalized aerodynamic roughness for the grassland stands at 0.15 [27]. Taking the height of grassland vegetation, with a value of 0.2 m, yields an aerodynamic roughness length of 0.03 m for the grassland.

Based on meteorological data, peak wind velocities in the region typically manifest in January, coinciding with minimal vegetation cover across agricultural landscapes, where the aerodynamic roughness length is measured at 0.0026 cm [28]. Under conditions where the peak wind speed coincides with January, the aerodynamic roughness of farmland is presumed to be equivalent to that of bare ground. In regions A and B, an ascertainment of the average aerodynamic roughness yields a measure of 0.023 m.

**Table 1.** Land types.

IGBP	Typology	Region A			Region B		
		Area (km <sup>2</sup> )	Percentage	Roughness	Area (km <sup>2</sup> )	Percentage	Roughness
10	Grasslands	18.71	74.87%	0.03 (m)	18.62	74.12%	0.03 (m)
12	Croplands	1.46	5.84%	0.0026 (cm)	0.53	2.11%	0.0026 (cm)
16	Bareen	4.82	19.29%	0.0026 (cm)	5.97	23.77%	0.0026 (cm)
Total		24.99	100%	0.023 (m)	25.12	100%	0.023 (m)

Within the computational framework of Fluent for addressing wall-related phenomena, the selection of the roughness height is a critical parameter. Thus, the conversion of the roughness length,  $z_0$ , to its commensurate roughness height, ' $h$ ', becomes imperative. Across diverse surface cover scenarios, a consistent linear relationship governs between the roughness length,  $z_0$ , and the resultant roughness height, ' $h$ ', succinctly expressed as  $h = \alpha z_0$ . Parameter ' $\alpha$ ' serves as the conversion factor between the two distinct roughness characterization parameters, contingent upon the nature of surface coverage. In the instance of grass cover within this study, the conversion factor ' $\alpha$ ' linking the roughness height to the roughness length,  $z_0$ , is determined to be 7.5 [29].

### 3.2. Thermal Parameters of Air

Most of the solar greenhouses in Tibet are located at an altitude of 2500 m to 4000 m, where the air is relatively thin. Air density is the primary parameter related to air pressure and is expressed as [30]

$$\rho = \frac{p \times 10^2}{RT} \left( 1 - 0.378 \frac{e}{p} \right) \quad (1)$$

where  $\rho$  is the air density at the reference elevation;  $T = 273.15 + t$ ,  $R = 287.05$ ; and  $e$  is the water vapor pressure.  $p$  is the value of air pressure at the reference elevation, which can be expressed as

$$p = p_0 \times \left( 1 - \frac{0.0065h}{288.15} \right)^{5.25588} \quad (2)$$

where  $p_0$  is the standard atmospheric pressure with a value of 1013.25 hPa;  $h$  is the elevation of the reference altitude layer.

The dew point temperature in Lhasa reached  $-4.1$  °C [30], the water pressure was equal to the saturated water pressure at the water surface, and the altitude was taken as 3658 m [31]. The average annual temperature of the Tibetan Plateau is  $-5.6$ ~ $3.8$  °C, and  $t$  was taken as  $3$  °C. The atmospheric pressure in Lhasa was 64.437 kPa, the air density  $\rho$  was  $0.809$  kg/m<sup>2</sup>, and the viscosity was taken as  $2.19 \times 10^{-5}$  m<sup>2</sup>/s [30].

### 3.3. Gravitational Acceleration

The value of gravitational acceleration is closely related to latitude and altitude. The gravitational acceleration at an altitude of 0 m at a certain latitude can be obtained from Equation (3). Then, the resulting value can be corrected for altitude using Equation (4) to obtain the value of gravity, taking latitude and altitude into account [32].

$$g_{\phi,1980} = 9.780327 \left( 1 + 0.00530244 \sin^2 \phi - 0.00000585 \sin^2 2\phi \right), \quad (3)$$

$$dg/dh = -3.08769 \times 10^{-6}(1 - 0.0014437 \sin^2 \phi) \quad (4)$$

where  $\phi$  is the latitude;  $dg/dh$  is the value for the change in gravity with height. The altitude of Lhasa was taken as 3568 m, the latitude was taken as 29.6° N, and the calculated acceleration of gravity was 9.78 m/s<sup>2</sup>.

### 3.4. Wall Functions and Meshing

In CFD numerical simulations, the modeling of intricate surfaces typically involves two primary methodologies [33]: the utilization of the wall function method and the integration of resistance source terms within the computational domain. Researchers have observed a close correspondence between simulated wind speed outcomes and actual measurements when employing wall functions for wind field simulations within intricate terrains. This alignment between simulated and empirical wind speed data highlights the accuracy achieved through the utilization of wall functions in complex terrain simulations. In this paper, the wall function method is used for wind field simulation in complex terrain. The wall function within Fluent is an empirically derived relationship, crafted through fitting the experimental dataset of fully developed rough pipe flow [18]. This relationship hinges upon the parameter ' $h$ ', representing air roughness height, which directly corresponds to the physical diameter of the sand grains employed in the experimental setup. The implementation of the wall function necessitates simultaneous fulfillment of a minimum of three essential criteria [34]:

(1) A high-resolution, near-wall vertical mesh is an indispensable prerequisite in computational fluid dynamics investigations, crucial for capturing precise flow characteristics within turbulent boundary layers. Its meticulous implementation ensures an accurate representation of turbulent flow dynamics. (2) The vertical separation denoted as ' $y_p$ ', measured from the center of mass within the initial grid layer to the underlying surface, exceeds the physical height parameter of the input roughness, ' $h$ '. (3) The relationship between the physical height of roughness  $h$  and the length of air roughness  $z_0$  [18]:

$$h \approx \frac{9.793}{C_s} z_0 \quad (5)$$

where  $K_s$  is the roughness height, m;  $z_0$  is the roughness length, m; and  $C_s$  is the roughness constant. The default in Fluent is 0.5.

Considering parameters such as computer hardware specifications, simulation accuracy, and maximum roughness within the setup and drawing insights from the relevant literature [33], the initial grid height for the boundary layer in the study area was set at 1 m. The body mesh exhibited a growth rate of 1.1, with the maximum grid size for the ground set at 5 m and for the remaining areas at 100 m. The cumulative grid count for the two regions approximated 40 million.

The determination of greenhouse wind loads necessitates precise wind speed data at intervals of 3 s, aligned with a 20-year return period. Consequently, the wind velocity was set at 35.6 m/s at a height of 10 m. The inlet boundary conditions were defined using an exponential rate function while considering the geomorphological classification as class B, with a corresponding coefficient ( $\alpha$ ) value of 0.15. The mathematical representation of the inlet wind speed profile is delineated in Equation (6). Parameters related to the turbulence dissipation rate adhere to established Japanese norms. The simulation of the wind field was conducted within area A. The wind speed and turbulence kinetic energy parameters at the outlet boundary of area A were transmitted via the Profile file. These values were subsequently adopted as the inlet boundary conditions for region B. Conspicuously, the wind speed and turbulent kinetic energy data at the outlet boundary of region A served as the prescribed inlet conditions for region B. For the outlet boundaries of both regions A and B, a pressure outlet configuration was employed. Symmetric boundary conditions were applied to the lateral and upper extents of the computational domain. Wall boundary

conditions were implemented for valleys and mountains. The roughness scores for both regions' wall boundaries were uniformly set to 0.17 m.

$$V_z = 35.6 \left( \frac{z}{z_0} \right)^{0.15} \quad (6)$$

The turbulence model RNG  $k-\epsilon$  was selected for numerical simulations. The SIMPLE algorithm addresses the challenge by delineating the pressure correction and velocity correction steps, offering a balance between stability and computational expense, rendering it well-suited for a wide array of flow scenarios. In contrast, the COUPLE algorithm synchronously updates pressure and velocity fields within each iteration, presenting a streamlined and immediate iterative approach when juxtaposed with SIMPLE. The COUPLE algorithm was used in region A, and the SIMPLE algorithm was used in region B due to computer hardware and accuracy limitations.

### 3.5. Analysis of Wind Speed Ratio at Different Heights

This study introduces the concept of the wind speed ratio to assess the impact of valley topography on wind speed variation across different locations within the basin. Specifically, the wind speed ratio is defined as the scalar ratio of the wind speed at various points within the basin to that recorded at a height of 10 m at the entrance of region A, serving as a reference point for comparative analysis. Cloud maps depicting plane wind speeds were captured at five distinct altitude levels, with corresponding wind speed ratio representations showcased in Figure 8 for region A and Figure 9 for region B.

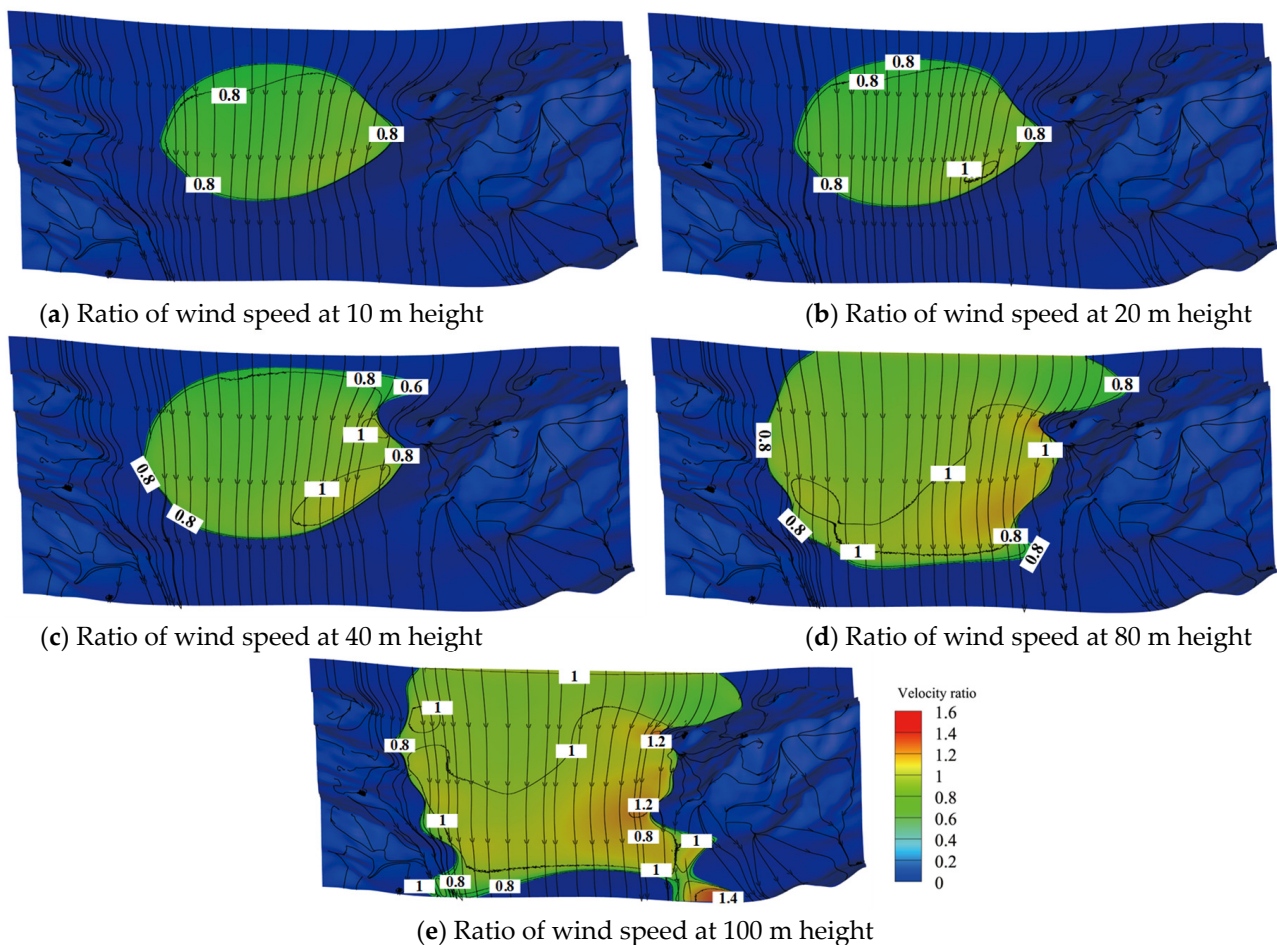
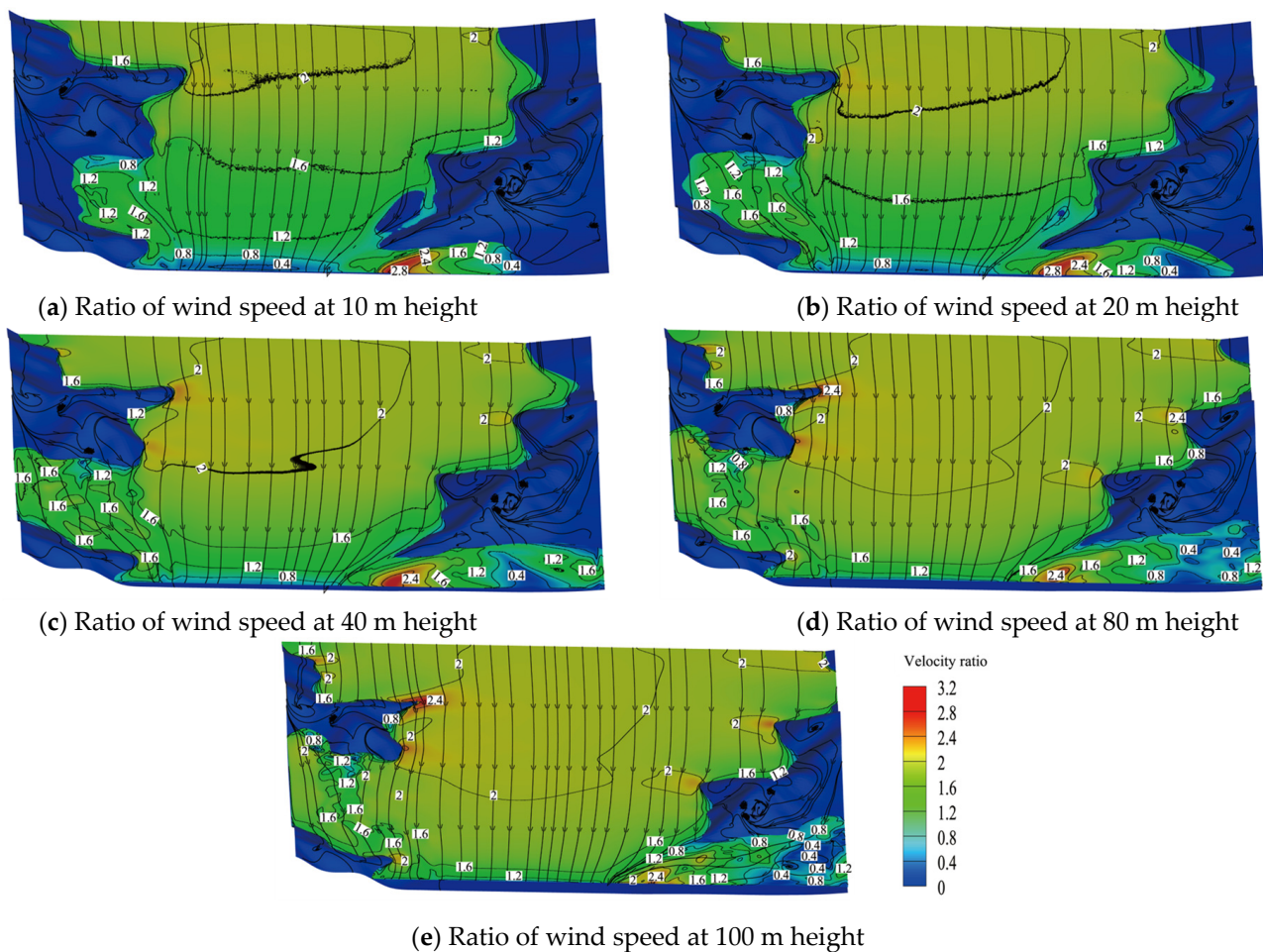


Figure 8. Ratio of wind speeds at different heights in region A.



**Figure 9.** Ratio of wind speeds at different heights in region B.

Analysis of the figures revealed a pronounced acceleration effect of the valley on the wind speed, notably culminating in maximum velocities proximal to the B area's exit, as evidenced by a wind speed ratio of 2.4. At elevated altitudes above ground level, both area A and area B exhibit elevated wind speed ratios, characterized by diminished ratios on the leeward side of the mountain compared to the windward side. In closer proximity to the mountain, wind speed ratios demonstrate a tendency toward smaller magnitudes. Given the direct correlation between wind load and wind speed, prudent site selection for construction within valleys entails proximity to mountainous terrain, particularly areas sheltered from prevailing winds. Furthermore, it is noteworthy that taller structures within valleys are inherently more susceptible to heightened wind loads compared to their lower counterparts.

## 4. Results and Discussion of Wind Load in Solar Greenhouse Group

### 4.1. Greenhouse Group Flow Field

The calculation domain parameters for the solar greenhouse group encompass specifications: a perpendicular size to incoming flow ( $\geq 9L$ ), a row-to-incoming flow size ( $\geq 10W$ ), and a height ( $\geq 5H$ ). Here,  $L$  denotes the length of the building perpendicular to the incoming flow in meters (m),  $W$  represents the length of the building parallel to the incoming flow in meters (m), and  $H$  signifies the height of the building in meters (m). To ensure adequate flow field development, the greenhouse group model was positioned within the windward and forward one-third sections of the calculation domain. The solar greenhouse group was configured along an east–west axis, aligned parallel to the valley. This arrangement assumes a wind angle of  $0^\circ$  concerning the north wall of the solar greenhouse, perpendicu-

lar to the incoming flow. Additionally, an incoming wind angle of  $94^\circ$  was considered in relation to the greenhouse group. Considering the greenhouse group as a unified entity, its dimensions span  $L_x$  (length) at 195 m,  $D_z$  (width) at 69 m, and  $H$  (height) at 5.5 m. For this study, the calculation domain dimensions for the greenhouse group were set to  $10L_x$  in the length direction,  $9D_z$  in the width direction, and 100 m in the height direction, as shown in Figure 10.

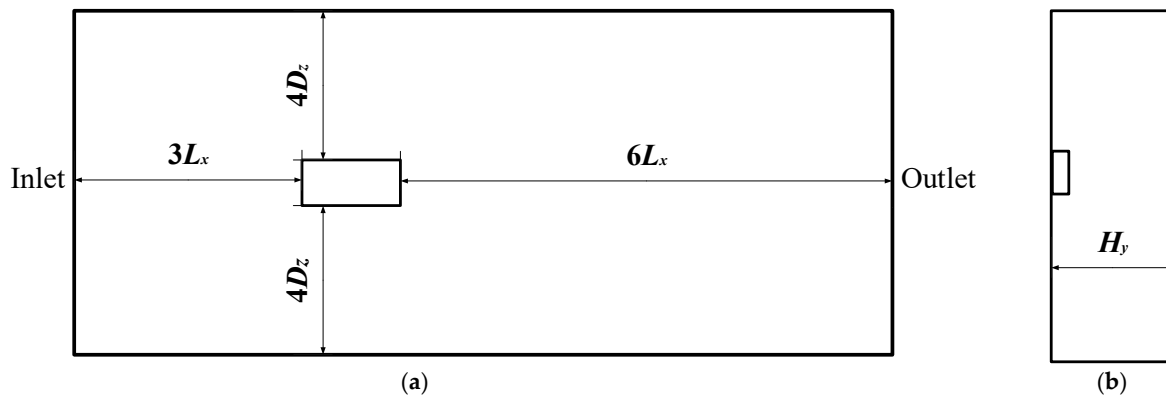


**Figure 10.** Greenhouse group calculation domain dimensions. (a) Plan dimensions of the calculation field of the solar greenhouse fluid domain. (b) Vertical dimensions of the calculation field of the solar greenhouse fluid domain.

#### 4.2. Boundary Conditions and Turbulence Modelling

The near-surface wind speed parameters for the entire region B were derived from simulations conducted on the wind fields of both region A and region B. The inlet wind speed for subsequent wind load simulations was determined by extracting the wind speed at the specific latitude and longitude coordinates corresponding to the location of the greenhouse group in region B. The wind speed profiles obtained by fitting are shown in Figure 11, using the fitted equation:

$$V = (b + c \times y) / (1 + a \times y) \quad (7)$$

where  $y$  is the height;  $a = 0.39785$ ,  $b = 0.23276$ , and  $c = 30.2164$ ; and the fitted  $R^2$  is 0.99424. At an altitude of 10 m above the surface, the inlet wind exhibits a direction of  $4^\circ$  east-southeast relative to the valley. Simultaneously, the solarium group was aligned parallel to the valley, resulting in an incoming wind direction for the solarium group that deviated by  $94^\circ$ .

The inlet boundary condition was determined by employing the wind speed profile, as defined by Equation (7). The values for parameters, specifically the turbulent dissipation rate and turbulent kinetic energy, adhere to Japanese specifications. Subsequently, wind speed profiles, turbulent kinetic energy profiles, and turbulent dissipation rate profiles were integrated into Fluent using UDF programming. A pressure outlet was used for the outlet boundary. Symmetrical boundaries were used for both side and top boundaries. Wall conditions were used for the bottom and solar greenhouse surface boundaries. A simulation of wind pressure acting on the surface of the solar greenhouse was conducted by employing realizable  $k-\varepsilon$  models and non-equilibrium wall functions.

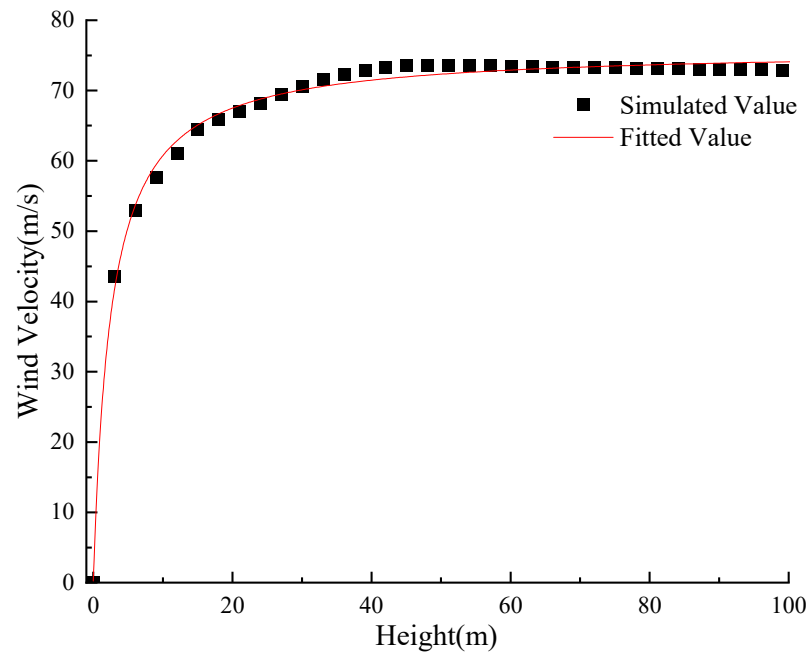


Figure 11. Simulated inlet wind speeds for greenhouse groups.

#### 4.3. Surface Wind Pressure Coefficient for Greenhouse Group

As can be seen in Figure 12, the windward side is the east end wall of greenhouses 1-1, 2-1, and 3-1. The wind pressure coefficient within the central region of the windward facade manifests as positive, with the apex of this positive coefficient exceeding 0.6. Conversely, an inversely signed wind pressure coefficient is observed along the eastern end wall near the leading edge of the frontal roof, reaching a minimum value of  $-0.4$ .



Figure 12. Cloud chart of wind pressure coefficient distribution on the surface of the solar greenhouse group.

Substantial negative wind pressure coefficients are evident along the front and rear roofs, as well as the northern periphery of the solar greenhouse proximal to the incoming flow. Notably, extreme values in these regions can be as low as  $-1.4$ . In contrast, the wind pressure coefficients across the remaining sections of the roof and north wall exhibit a range from 0 to  $-0.2$ . The absolute value of the wind pressure coefficient increases in proximity to the incoming flow, while within the vicinity of the outgoing flow, the absolute value

of the wind pressure coefficient approximates 0. Due to the non-perpendicular nature of the incoming flow from the southeasterly wind, positive wind pressure coefficients are observed on the east end wall of greenhouses 1-1, 2-1, and 3-1, which are in close proximity to the incoming flow. Moreover, the east-end walls of the remaining greenhouses, particularly along their edges, exhibit distinct regions of positive wind pressure coefficients. It is notable, however, that the spatial distribution and extremities of these positive wind pressure coefficients differ among the greenhouses.

#### 4.4. Greenhouse Group Subdivision

The primary wind-resistant framework within the solar greenhouse comprises a transverse arch, wherein the predominant wind forces are exerted upon the north wall as well as the front and rear roofing structures. Consequently, this investigation centers on discerning the shape factors of the wind load specifically associated with the north wall, front roof, and rear roof. In accordance with the roof partitioning method delineated in the Chinese code [35], the anterior roof undergoes a symmetrical division into two equal segments based on horizontal projection. Subareas B, H, QS, and QX were arranged in a north-to-south sequence.

The internal structure of the solar greenhouse stems from the standard transverse arch spacing within the range of 0.8 m to 1.2 m, combined with the inherent susceptibility of the east and west extremities of the surface of the solar greenhouse to localized wind pressure coefficient peaks. The partitioning, which is the north wall and roofs of the solar greenhouse, follows a west–east labelling system, denoted as B, H, QS, and QX, as shown in Figure 13a. To manage this, the longitudinal 60 m segment was systematically divided into five lateral segments, resulting in a total of twenty distinct partitions, as shown in Figure 13b.

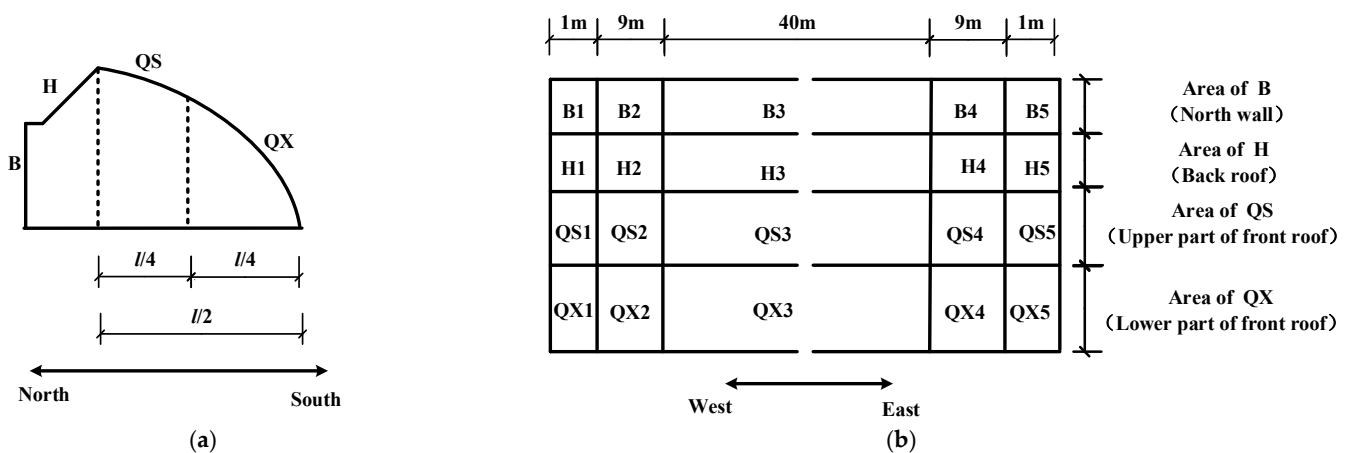


**Figure 13.** Surface zoning plan of solar greenhouse. (a) Plan view of north wall and roof partition. (b) Horizontal zoning map of greenhouse surface.

#### 4.5. Greenhouse Group Shape Factor of Wind Load

Table 2 provides shape factors of the wind load corresponding to each partition of both the north wall and the rear roof within the entirety of the greenhouse group. Observing Table 2, it is evident that the most pronounced negative shape factors of the wind load occur along the north wall and rear roof, particularly in proximity to the edge of the incoming flow. Furthermore, the shape factor of the wind load, distant from the region affected by the incoming flow, approaches a value of 0. Within the greenhouse complex, specific regions, denoted as B1 and B2 within greenhouses 1-1, 2-1, and 3-1 along the north wall and in close proximity to the incoming flow, exhibit prominent negative shape factors of wind load. These shape factors range from approximately  $-0.2$  to  $-0.5$ . Influenced by the wind angle and greenhouse arrangement, the B1 area of greenhouse 3-1 has a shape factor of wind

load of  $-0.50$ , which is less than the B1 area of greenhouse 2-1, which has a shape factor of wind load of  $-0.37$ , and less than the B1 area of greenhouse 1-1, which has a shape factor of wind load of  $-0.23$ . The absolute values of the shape factor of the wind load in the B3 to B5 regions range from 0 to 0.10. In the context of the greenhouse group, the rear surfaces of greenhouses 1-1, 2-1, and 3-1 situated in the H1 and H2 regions, proximal to the incoming airflow, exhibit outstanding negative shape factors of wind load. These shape factors range between  $-0.3$  and  $-0.4$ . However, the absolute values of the shape factors for greenhouses 1-1 of H1 and H2 were greater than the values for greenhouses 2-1 and 3-1.

**Table 2.** Shape factor of wind load for the north wall and rear roof zones of the greenhouse group.

Solar Greenhouse	B1	B2	B3	B4	B5	H1	H2	H3	H4	H5
1-1	-0.23	-0.29	-0.01	-0.06	-0.09	-0.41	-0.35	-0.03	0.04	0.06
1-2	-0.22	-0.07	0.01	0.02	0.01	-0.20	-0.06	0	0.01	0.01
1-3	-0.04	0	0.01	-0.01	-0.05	-0.07	-0.01	0	-0.01	-0.02
2-1	-0.37	-0.33	-0.01	0.06	0.04	-0.37	-0.34	0.02	0.04	-0.03
2-2	-0.18	-0.05	0.01	0.04	0.07	-0.15	-0.04	-0.01	0.02	0.06
2-3	-0.16	-0.02	-0.01	-0.02	-0.04	-0.22	-0.03	0	-0.02	-0.04
3-1	-0.50	-0.31	-0.01	0.02	0.02	-0.37	-0.31	-0.01	0.01	0.02
3-2	-0.09	0	0.03	0.08	0.07	-0.12	-0.01	0.03	0.07	0.12
3-3	-0.16	-0.09	-0.01	-0.03	-0.10	-0.22	-0.07	-0.02	-0.04	-0.09

The values of shape factors for each partition of the front roof of the greenhouse group are given in Table 3. The greenhouses denoted as 1-1, 2-1, and 3-1 are situated proximate to the inflow, manifesting substantial negative shape factors within the QS1 and QS2 regions. Remarkably, the magnitude of the negative shape factor within the QS1 region surpasses that within the QS2 region. Under the influence of wind direction and greenhouse layout, the absolute value of the QS1 shape factor for solar greenhouse 1-1 is determined to be 0.64, surpassing that of greenhouses 2-1 and 3-1. Meanwhile, the disparity in QS1 shape factors between greenhouses 2-1 and 3-1 is found to be minimal.

**Table 3.** Shape factors of wind load for front roofs in front of greenhouse group.

Solar Greenhouse	QS1	QS2	QS3	QS4	QS5	QX1	QX2	QX3	QX4	QX5
1-1	-0.64	-0.37	0	0.02	0.02	-0.75	-0.29	-0.01	0.04	-0.03
1-2	-0.05	-0.03	0.01	0.02	0.02	-0.05	-0.03	0	0.02	0.02
1-3	-0.05	-0.01	0	-0.01	-0.03	-0.04	0	0.01	-0.02	-0.07
2-1	-0.44	-0.35	-0.01	0.01	0	-0.59	-0.32	-0.01	0	-0.12
2-2	-0.10	-0.01	0.02	0.03	0.03	-0.07	0.02	0.03	0.05	0
2-3	-0.08	-0.04	-0.01	-0.02	-0.04	-0.14	-0.04	-0.01	-0.02	-0.05
3-1	-0.46	-0.32	-0.01	0.02	0.04	-0.51	-0.26	0.01	0.02	0
3-2	-0.10	0	0.02	0.03	0.04	-0.04	0.02	0.02	-0.02	-0.21
3-3	0.02	0	0	-0.03	-0.10	-0.06	0.03	0.01	-0.03	-0.10

The values of the shape factors for the three greenhouse QS2 regions are close to each other, with values around  $-0.35$ . The absolute values of the shape factors for the remaining greenhouse areas range from about 0 to 0.10. The distribution pattern of shape factors within the lower segment of the front roof mirrors that observed in the upper segment. However, distinct variations emerge as the absolute values of QX1 shape factors exhibit a 10.9% to 34% augmentation in comparison to QS1. Markedly, the absolute values of shape factors for QX2 demonstrate a noteworthy reduction, ranging from 8.5% to 21%, relative to QS2. Moreover, an overarching trend is evident in the greenhouse structure, where the absolute values of the shape factor along the entire perimeter exceed those found in the central region.

## 5. Results and Discussion of 0° Wind Angle

### 5.1. Analysis of Wind Pressure Coefficients

In the preceding section, the surface wind pressure coefficient and shape factor for wind loads on a solar greenhouse were derived, specifically considering wind angles approximating 90°. Nevertheless, drawing upon insights from prior investigations, it is worth noting that a wind angle of 0° is identified as unfavorable for solar greenhouses, based on empirical observations. In this section, a simulation of surface wind pressure experienced by the greenhouse group is conducted, with particular emphasis on selecting a wind angle of 0° for the simulation. The resultant surface wind pressure coefficients corresponding to the greenhouse group under a 0° wind angle are illustrated in Figure 14.

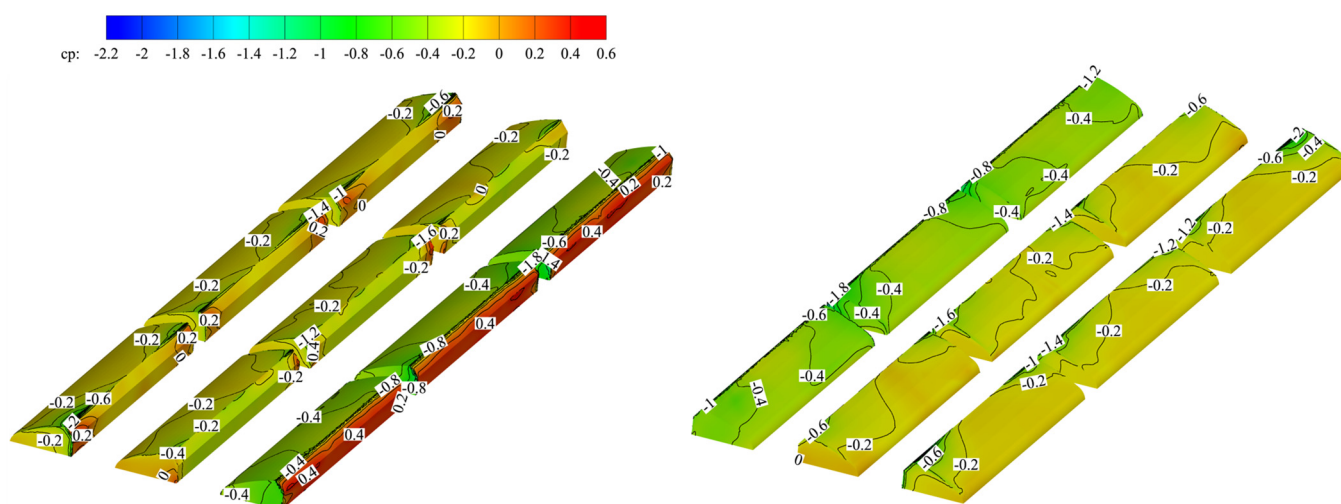


**Figure 14.** Cloud chart of the wind pressure coefficient on the surface of the solar greenhouse group under a 0° wind direction angle.

As illustrated in Figure 14, the windward aspect corresponds to the northern wall and rear roofing of greenhouses 1-1 to 1-3. Predominantly, the positive wind pressure envelops the expansive windward surfaces, with the peak positive wind pressure surpassing 0.4. The peripheral region on the windward side exhibits a discernible zone of negative wind pressure, exemplified by the area proximate to the rear roof adjacent to the ridge. In this particular location, the negative wind pressure coefficient attains a maximum value of approximately  $-1.8$ . The majority of the front roofs in greenhouses 1-1 to 1-3 exhibit wind pressure coefficients hovering around  $-0.4$ , while the roofs and north walls of the remaining greenhouses predominantly display wind pressure coefficients ranging between 0 and  $-0.2$ . Nevertheless, discernible positive wind pressure is noted at specific edges, exemplified by a wind pressure coefficient reaching up to 0.2 along the eastern and western perimeters of the northern and western walls of the rear roofs spanning greenhouses 2-1 to 3-3. In relation to negative wind pressure coefficients along the ridge, there is a notable aggregation of such coefficients spanning the ridge of the initial row of greenhouses, extending seamlessly from east to west. Additionally, a concentration of wind pressure coefficients is observed along the ridge of the final two rows of greenhouses, specifically localized at the eastern and western extremities of the ridge. However, the zone characterized by concentrated negative wind pressure within the middle greenhouse not only exhibits limited spatial coverage and a large negative wind pressure coefficient but also underscores the distinctive nature of the concentration area of negative wind pressure within the rear greenhouse. This specific region, situated between the first two rows of greenhouses, attains an extreme negative wind pressure value, reaching as low as  $-2$ .

### 5.2. Analysis of Shape Factor of Wind Load

Table 4 presents the shape factor of wind load corresponding to individual partitions of both the north wall and rear roof within the solar greenhouse group, under 0° wind direction. The shape factors of the greenhouse group in each partition of each row are about east–west symmetrical. The inaugural row of greenhouses (denoted as 1-1 to 1-3) exhibited predominantly positive shape factors across the northern wall and rear roof regions. Moreover, the shape factors within the B2 to B4 regions of the greenhouses demonstrate a notable convergence, exhibiting values approximately around 0.30. The first row of greenhouses exhibits a negative shape factor within the peripheral area, and the absolute value of the shape factor at the edge of the central greenhouse surpasses that of the remaining two structures.

**Table 4.** The shape factors of the wind load for the north wall of the greenhouse group and the rear roof for each partition under 0° wind direction.

Solar Greenhouse	B1	B2	B3	B4	B5	H1	H2	H3	H4	H5
1-1	−0.10	0.28	0.33	0.31	−0.01	−0.03	0.16	0.15	0.11	−0.04
1-2	−0.12	0.28	0.32	0.30	−0.13	−0.10	0.04	0.12	0.05	−0.15
1-3	−0.07	0.29	0.32	0.24	−0.03	−0.05	0.11	0.16	0.13	0.03
2-1	−0.04	−0.27	−0.31	−0.20	0.01	−0.08	−0.24	−0.28	−0.21	0.03
2-2	0.08	−0.12	−0.29	−0.09	0.13	0.11	−0.17	−0.27	−0.18	0.19
2-3	0.07	−0.20	−0.30	−0.22	−0.09	0.07	−0.19	−0.26	−0.14	−0.09
3-1	0.04	0.18	−0.11	0.02	−0.11	0.04	0.02	−0.13	0.01	0.03
3-2	−0.08	0.01	−0.13	0.05	−0.11	0.06	0	−0.15	0	0.02
3-3	−0.12	0.02	−0.10	0.14	0.06	−0.04	0.05	−0.12	−0.01	0.01

The central section of the northern wall within the intermediate greenhouses (designated as 2-1 to 2-3) exhibits a distinct negative shape factor of wind load. Specifically, each greenhouse demonstrates a shape factor of approximately −0.30 for regions B3 and H3, while areas B2 and B4 display a shape factor of wind load of around −0.20 in greenhouses 2-1 and 2-3. Conspicuously, greenhouse 2-2 manifests a pronounced negative shape factor of approximately −0.10 for regions B2 and B4. In the final row of greenhouses (designated as 3-1 to 3-3), shape factor values were consistently observed at approximately −0.11 within the B3 and H3 regions. Certain areas exhibited shape factors in close proximity to zero.

From Table 5, the shape factor for each section of the front roof within the greenhouse group registered values below 0. Remarkably, within the QS3 area for each individual greenhouse in the greenhouse group, the absolute magnitude of the shape factor was notably lower than that observed in the remainder of the area. Prominent instances of large absolute values in negative shape factors were predominantly identified within the peripheries of the greenhouse structures. Markedly, specific locations, such as areas QS1 and QS5 within greenhouse 1-2, exhibited notable absolute values of shape factors, measuring 0.6 and 0.72, respectively.

The absolute magnitudes of the shape factors within the QX region of the greenhouses are consistently smaller than those observed in the QS region. Notably, in the initial row of greenhouses adjacent to the incoming flow (region QX2 to QX3), the shape factors demonstrated close numerical proximity. Additionally, within each subdivision, the absolute values of the shape factors in the leading row of daytime greenhouses surpassed those observed in the subsequent two rows. In all zones, the second row of greenhouses displayed closely aligned values of shape factors. Particularly, within the third row of greenhouses, specifically zones QX5 and QX1 in greenhouse 3-1, significant negative shape factors were observed.

**Table 5.** The shape factors of the wind load for each partition of the front roof of the greenhouse group under 0° wind direction.

Solar Greenhouse	QS1	QS2	QS3	QS4	QS5	QX1	QX2	QX3	QX4	QX5
1-1	−0.54	−0.48	−0.38	−0.49	−0.58	−0.45	−0.42	−0.38	−0.42	−0.53
1-2	−0.60	−0.55	−0.37	−0.63	−0.72	−0.49	−0.40	−0.35	−0.41	−0.56
1-3	−0.62	−0.51	−0.37	−0.50	−0.46	−0.56	−0.44	−0.37	−0.37	−0.37
2-1	−0.33	−0.32	−0.21	−0.27	−0.44	−0.17	−0.14	−0.17	−0.16	−0.21
2-2	−0.47	−0.34	−0.23	−0.37	−0.51	−0.23	−0.19	−0.19	−0.20	−0.27
2-3	−0.37	−0.27	−0.20	−0.34	−0.32	−0.15	−0.13	−0.17	−0.14	−0.15
3-1	−0.58	−0.57	−0.22	−0.33	−0.35	−0.30	−0.18	−0.15	−0.16	−0.18
3-2	−0.39	−0.31	−0.23	−0.40	−0.42	−0.21	−0.18	−0.16	−0.19	−0.19
3-3	−0.30	−0.32	−0.20	−0.51	−0.51	−0.17	−0.15	−0.15	−0.16	−0.25

## 6. Results and Discussion of Group Effect

In order to unveil the influence of the interference effect exerted by solar greenhouse groups and to elucidate the intricate patterns of wind pressure fluctuations across their surfaces, the interference factor, denoted as  $IF_{\mu}$  [36], was introduced, with its mathematical expression provided in Equation (8):

$$IF_{\mu} = \frac{\mu_{sI}}{\mu_{sA}} \quad (8)$$

where  $\mu_{sI}$  represents the shape factors of the wind load of each partition within the greenhouse group under the influence of interference effects, and  $\mu_{sA}$  represents the shape factors of the wind load of corresponding partitions within individual greenhouses unaffected by such disturbances. The proportional relationship between the two reflects the degree to which wind interference effects influence the system.

Specifically, when the absolute value of  $IF_{\mu}$  exceeds 1.0, it manifests as an amplification effect induced by the presence of the solar greenhouse group. In this scenario, wind loads escalate, with the magnitude of amplification increasing proportionally with the absolute value of  $IF_{\mu}$ . When the absolute value of  $IF_{\mu}$  falls below 1.0, it is indicative of a shading effect induced by the presence of the solar greenhouse group. In this scenario, wind loads diminish, with the prominence of the shading effect increasing as the absolute value decreases. When  $IF_{\mu}$  equals 1.0, the interference effect dissipates, resulting in wind loads akin to those experienced in a solitary solar greenhouse scenario. Conversely, if  $IF_{\mu}$  is less than 0, it signifies a reversal in wind direction induced by the interference effect.

### 6.1. Solar Greenhouses in River Valleys

Table 6 reveals a notable trend across the greenhouse group, wherein the interference factors (regions B1 and B2) for greenhouses 1-1, 2-1, and 3-1, positioned proximal to the leading edge of the incoming flow, surpass those observed in analogous regions of the remaining greenhouses. Excluding greenhouse 1-1, where the interference factor measured below 1.0 within sector B1, the adjacent two greenhouses registered interference factors surpassing 1.0 within the identical zone.

Among the trio of greenhouses positioned proximate to the incoming airflow, greenhouse 3-1 occupies the foremost position along the windward alignment. Despite lacking direct shading in its forward expanse, the interference factor within its B1 region stood notably elevated at 1.39, rendering it susceptible to pervasive interference from neighboring greenhouses. Being situated in the rearmost row on the windward side, greenhouse 1-1 experienced the most pronounced shading influence. Evidently, its interference factor registered at a mere 0.64, elucidating the conspicuousness of the shading effect. The interference factors observed within the B2 and H2 sectors of the three greenhouses situated along the windward front row exhibited a range of 1.01 to 1.18, indicative of minimal amplification effects. Statistical analysis revealed that these effects did not attain significance. Conversely, the interference factor within the remaining subdivisions of the aforementioned

three greenhouses, as well as within each sector of the remaining solar greenhouse regions, consistently registered values below 1.0.

**Table 6.** Interfering factor for the north wall and rear roof zones of the greenhouse group.

Solar Greenhouse	B1	B2	B3	B4	B5	H1	H2	H3	H4	H5
1-1	0.64	1.01	0.25	1.18	0.96	0.69	1.18	0.59	−0.70	−0.63
1-2	0.61	0.24	−0.25	−0.39	−0.11	0.34	0.20	0.00	−0.17	−0.10
1-3	0.11	0.00	−0.25	0.20	0.53	0.12	0.03	0.00	0.17	0.21
2-1	1.03	1.15	0.25	−1.18	−0.43	0.62	1.15	−0.39	−0.70	0.31
2-2	0.50	0.17	−0.25	−0.79	−0.75	0.25	0.13	0.20	−0.35	−0.63
2-3	0.44	0.07	0.25	0.39	0.43	0.37	0.10	0.00	0.35	0.42
3-1	1.39	1.08	0.25	−0.39	−0.21	0.62	1.05	0.20	−0.17	−0.21
3-2	0.25	0.00	−0.75	−1.57	−0.75	0.20	0.03	−0.59	−1.22	−1.26
3-3	0.44	0.31	0.25	0.59	1.07	0.37	0.24	0.39	0.70	0.94

From Table 7, it is evident that the highest interference factor value within each partition of the front roof of the greenhouse group is localized to the QX5 region of greenhouse 3-2, registering at a magnitude of 2.79. Additionally, by referencing Table 3, it becomes apparent that the windward-facing greenhouses in the front row, namely QS1, QS2, QX1, and QX2, exhibit significant negative wind pressure coefficients. Consequently, a thorough analysis of the interference factor distribution in these specified regions becomes imperative.

**Table 7.** Interfering factor for front roofs in front of greenhouse group.

Solar Greenhouse	QS1	QS2	QS3	QS4	QS5	QX1	QX2	QX3	QX4	QX5
1-1	0.98	1.38	0.00	−0.41	−0.20	1.34	1.37	0.32	−0.95	0.40
1-2	0.08	0.11	−0.27	−0.41	−0.20	0.09	0.14	0.00	−0.48	−0.27
1-3	0.08	0.04	0.00	0.20	0.31	0.07	0.00	−0.32	0.48	0.93
2-1	0.67	1.31	0.27	−0.20	0.00	1.05	1.51	0.32	0.00	1.60
2-2	0.15	0.04	−0.53	−0.61	−0.31	0.12	−0.09	−0.96	−1.19	0.00
2-3	0.12	0.15	0.27	0.41	0.41	0.25	0.19	0.32	0.48	0.67
3-1	0.70	1.20	0.27	−0.41	−0.41	0.91	1.23	−0.32	−0.48	0.00
3-2	0.15	0.00	−0.53	−0.61	−0.41	0.07	−0.09	−0.64	0.48	2.79
3-3	−0.03	0.00	0.00	0.61	1.02	0.11	−0.14	−0.32	0.71	1.33

The interference factors within the QS1 and QS2 regions of the windward-facing greenhouses' front row exhibit magnitudes exceeding those observed within the corresponding regions of the remaining greenhouse. Particularly noteworthy is the interference factor within the QS1 region of the windward front row greenhouses, which uniformly falls below 1.0, with the exception of the QS1 region of greenhouse 1-1, where the interference factor registers at 0.98, indicating a relatively weak shading effect. Shading effects are observed in the QS1 region of greenhouses 2-1 and 3-1, characterized by interference factors of 0.67 and 0.70, respectively. In the QS2 region, the shape factors for greenhouses 1-1, 2-1, and 3-1 are, respectively, 1.38, 1.31, and 1.20 times greater than those observed in the corresponding regions of individual solar greenhouses, indicative of a notable amplification effect when compared to individual greenhouse.

The interference factor within the QX2 region of the windward front row surpasses 1.0, with greenhouse 2-1 exhibiting the highest value at 1.51 and greenhouse 3-1 registering the lowest at 1.23. However, the distribution pattern of interference factors within the QX1 region of the windward front row of greenhouses deviates from that observed in region QX2. While greenhouses 2-1 and 3-1 exhibit interference factors near 1.0, shading effects are evident in greenhouse 3-1, with greenhouse 2-1 demonstrating an amplification effect.

## 6.2. 0° Wind Angle

Table 8 illustrates that the interference factor values within each greenhouse H5 region of the greenhouse group vary between  $-65.43$  and  $51.56$ . This variability arises from the shape factor of a single greenhouse, H5, at a wind angle of  $0^\circ$ , which is measured at  $0.0029$ . In Table 4, the shape factors for the H5 partitions of greenhouse 1-2 and greenhouse 2-2 are noted as  $-0.15$  and  $0.19$ , respectively. Notably, the absolute values of shape factors within the same regions of the remaining greenhouses are all below  $0.09$ . A critical imperative emerges to elucidate the distribution patterns of interference factors across the remaining regions.

**Table 8.** Interfering factor for the north wall of the greenhouse group and the rear roof for each partition under  $0^\circ$  wind direction.

Solar Greenhouse	B1	B2	B3	B4	B5	H1	H2	H3	H4	H5
1-1	3.08	0.90	0.80	0.95	0.36	1.30	1.33	0.88	0.78	13.77
1-2	3.69	0.90	0.78	0.92	4.69	4.33	0.33	0.71	0.36	51.65
1-3	2.15	0.93	0.78	0.74	1.08	2.16	0.91	0.94	0.92	$-10.33$
2-1	1.23	$-0.87$	$-0.75$	$-0.61$	$-0.36$	3.46	$-1.99$	$-1.65$	$-1.49$	$-10.33$
2-2	$-2.46$	$-0.39$	$-0.70$	$-0.28$	$-4.69$	$-4.76$	$-1.41$	$-1.59$	$-1.28$	$-65.43$
2-3	$-2.15$	$-0.64$	$-0.73$	$-0.68$	3.24	$-3.03$	$-1.58$	$-1.53$	$-1.00$	30.99
3-1	$-1.23$	0.58	$-0.27$	0.06	3.97	$-1.73$	0.17	$-0.77$	0.07	$-10.33$
3-2	2.46	0.03	$-0.32$	0.15	3.97	$-2.60$	0.00	$-0.88$	0.00	$-6.89$
3-3	3.69	0.06	$-0.24$	0.43	$-2.16$	1.73	0.41	$-0.71$	$-0.07$	$-3.44$

The front-row windward greenhouses, specifically the B2 to B4 regions of greenhouses 1-1 to 3-1, exhibit shape factor values ranging from  $0.74$  to  $0.95$  times higher than those observed in the corresponding regions of individual greenhouses. Despite the absence of shading structures in front of these greenhouses, discernible shading effects persist. In each greenhouse within the second row (greenhouses 2-1 to 2-3), the  $IF_\mu$  values for the B2 to B4 region exhibit absolute magnitudes falling between  $0.0$  and  $-1.0$ . This range implies the occurrence of both shading effects resulting from the front greenhouse's shadow and a reversal in wind direction. The B3 region of greenhouses in the third row (greenhouses 3-1 to 3-3) exhibit a notably pronounced influence from shading effects, as evidenced by interference factors ranging between  $-0.24$  and  $-0.32$ . The B2 region of greenhouse 3-2 and the B4 region of greenhouse 3-3 exhibit discernible shading effects; however, the shape factor values within these regions are approximately half of those observed in individual greenhouses. In contrast, the B2 and B4 regions of the remaining greenhouses in the third row display maximum interference factors of only  $0.15$ . The overwhelming majority of greenhouses within the group exhibit interference factors exceeding  $1.0$  along the northern wall's periphery. Despite an amplification effect, the shape factor within these regions is comparably diminished in comparison to the central segment of the northern wall. Furthermore, it is imperative to highlight the occurrence of wind direction inversion within the B1 and B5 regions of greenhouses, spanning from 2-1 to 2-3.

In the realm of the rear roof, shading phenomena are observed within the H2 to H4 sectors of the three greenhouse structures proximal to the incoming flow, with a discernibly greater intensity of shading evident in greenhouse 1-2 compared to its counterparts. Greenhouse 1-2 exhibits an interference factor of merely  $0.71$  within the H3 region, while the shape factor pertaining to H2 and H4 is approximately one-third that of the singular greenhouse. The interference factor observed within the H2 to H4 sector of greenhouses 2-1 to 2-3 ranged from  $-1.0$  to  $0.99$ . The shading from the front greenhouse induces not only a shading effect but also a phenomenon of wind reversal. The three greenhouses situated farthest from the prevailing airflow exhibited interference factors of  $-0.77$ ,  $-0.88$ , and  $-0.71$  within their respective H3 regions. In contrast, the corresponding B2 and B4 regions within these greenhouses displayed a maximum interference coefficient of  $0.41$ , indicating a heightened susceptibility to shading effects in these areas.

The interference factors pertaining to the front roof consistently exceed 0. Examination of Table 9 reveals that the interference factors associated with each partition of the front row of windward greenhouses predominantly surpass 1. Remarkably, the interference factors within the edge regions, namely QS1, QS5, QX1, and QX5, surpass those observed in the central regions of the roof. This finding underscores the heightened amplification effect along the periphery of greenhouse groups. Nevertheless, certain regions exhibit interference factors below 1, exemplified by the QX4 sector within greenhouse 1-3, characterized by an interference factor of 0.90.

**Table 9.** Interfering factor for each partition of the front roof of the greenhouse group under 0° wind direction.

Solar Greenhouse	QS1	QS2	QS3	QS4	QS5	QX1	QX2	QX3	QX4	QX5
1-1	1.09	0.99	1.11	1.08	1.22	1.04	0.99	1.15	1.03	1.26
1-2	1.22	1.13	1.08	1.39	1.52	1.13	0.94	1.06	1.00	1.33
1-3	1.26	1.05	1.08	1.10	0.97	1.29	1.03	1.12	0.90	0.88
2-1	0.67	0.66	0.62	0.60	0.93	0.39	0.33	0.51	0.39	0.50
2-2	0.95	0.70	0.67	0.82	1.08	0.53	0.45	0.57	0.49	0.64
2-3	0.75	0.56	0.59	0.75	0.67	0.35	0.31	0.51	0.34	0.36
3-1	1.18	1.17	0.64	0.73	0.74	0.69	0.42	0.45	0.39	0.43
3-2	0.79	0.64	0.67	0.88	0.89	0.49	0.42	0.48	0.46	0.45
3-3	0.61	0.66	0.59	1.13	1.08	0.39	0.35	0.45	0.39	0.59

The interference factor within each area spanning greenhouses 2-1 to 2-3 remains below 1.0. Notably, the shading effect observed in greenhouse 3, situated centrally within the row of greenhouses, proves to be less pronounced compared to the corresponding areas of greenhouses 2-1 and 2-3. The shape factors exhibit amplification within the QS1 and QS2 sectors of greenhouse 3-1 and the QS4 and QS5 sectors of greenhouse 3-3, ranging from 1.08 to 1.18. However, a shading effect is observed along the remainder of the greenhouse row (greenhouses 3-1 to 3-3). While the pattern of interference factor alteration remains consistent across the upper and lower roofs within each greenhouse row, discernible differences in the degree of impact are evident.

In general, the upper segment of the anterior roof in the inaugural row experiences a more pronounced amplification compared to its lower counterpart, with interference factors for each segment of the latter approximating 1.0. The final two rows of greenhouses are susceptible to a shading effect, notably more prominent along the lower section of the anterior roof. Moreover, the lower portion of the third greenhouse row experiences the most substantial shading effect.

## 7. Conclusions

Analysis of the wind filed within the valley demonstrates a consistent trend: as altitude increases, wind speeds proportionally intensify. Furthermore, discernible disparities emerge between the windward and leeward aspects of the mountain, with the former exhibiting notably higher wind speeds in contrast to the latter.

Examination of wind pressure on the surface of a solar greenhouse group, organized in a configuration of three rows by three columns within a valley setting, elucidated significant insights. Special emphasis must be placed on the assessment of wind pressure coefficients and shape factors with the greenhouse structures, including the edge areas, roof ridges, and peripheral greenhouses within the greenhouse group. For instance, significant negative shape factors with substantial absolute values are observed along the front roof edge area of the greenhouse group under wind conditions at 0° wind direction.

Focusing on interference effects, the shape factors of the wind load exhibit amplification within the vicinity of the greenhouse edge region, proximal to the incoming flow. For example, there is an amplification effect in areas such as B1, B2, QX1, and QS1 in the front row of greenhouses close to the incoming flow at a wind direction of 94°. Of particular

interest is the observed reversal of the interference effect occurring at the north wall and front roof of the second row of greenhouses under wind direction at  $0^\circ$ . Given the negative shape factor of the frontal roof structure, heightened attention must be directed towards the amplification phenomenon occurring in the vicinity of the incoming airflow within greenhouse configurations.

The outcomes of these investigations offer valuable insights for informing the optimal siting of solar greenhouses within the Tibetan valley and for precision calculations of the surface wind load associated with each greenhouse within the group.

**Author Contributions:** Conceptualization, Z.L. and J.X.; software, Z.G.; investigation, R.W.; writing—original draft preparation, Z.G.; writing—review and editing, Z.L. and J.X.; visualization, Z.G. and Y.J.; data curation, R.W. and Y.J.; supervision, Z.L. All authors have read and agreed to the published version of the manuscript.

**Funding:** This research was funded by the National Natural Science Foundation of China (U20A2020) and the Beijing Innovation Consortium of Agriculture Research System (BAIC01-2023-20).

**Data Availability Statement:** Data is contained within the article.

**Conflicts of Interest:** The authors declare no conflicts of interest.

## References

1. Wang, Z.; Gong, D.; Zhang, Y. Investigating the effects of greenhouse vegetable cultivation on soil fertility in Lhasa, Tibetan Plateau. *Chin. Geogr. Sci.* **2020**, *30*, 456–465. [\[CrossRef\]](#)
2. Yang, Z.Q.; Li, Y.X.; Xue, X.P.; Huang, C.R.; Zhang, B. Wind loads on single-span plastic greenhouses and solar greenhouses. *HortTechnology* **2013**, *23*, 622–628. [\[CrossRef\]](#)
3. Jiang, Y.; Bai, Y.; Wang, C.; Wang, Y.; Pang, X. Dynamic response analyses of plastic greenhouse structure considering fluctuating wind load. *Adv. Civ. Eng.* **2021**, *2021*, 8886557. [\[CrossRef\]](#)
4. Moriyama, H.; Sase, S.; Kowata, H.; Ishii, M. Engineering analysis of the greenhouse structures damaged by typhoon 0221 in Chiba and Ibaraki. *J. Soc. Agric. Struct.* **2003**, *34*, 199–212. [\[CrossRef\]](#)
5. Kim, R.W.; Lee, I.B.; Yeo, U.H.; Lee, S.Y. Estimating the wind pressure coefficient for single-span greenhouses using an large eddy simulation turbulence model. *Biosyst. Eng.* **2019**, *188*, 114–135. [\[CrossRef\]](#)
6. Kwon, K.S.; Kim, D.W.; Kim, R.W.; Ha, T.; Lee, I.B. Evaluation of wind pressure coefficients of single-span greenhouses built on reclaimed coastal land using a large-sized wind tunnel. *Biosyst. Eng.* **2016**, *141*, 58–81. [\[CrossRef\]](#)
7. Song, J.L.; Li, J.W.; Flay, R.G. Field measurements and wind tunnel investigation of wind characteristics at a bridge site in a Y-shaped valley. *J. Wind Eng. Ind. Aerodyn.* **2020**, *202*, 104199. [\[CrossRef\]](#)
8. Jing, H.; Liao, H.; Ma, C.; Tao, Q.; Jiang, J. Field measurement study of wind characteristics at different measuring positions in a mountainous valley. *Exp. Therm. Fluid Sci.* **2020**, *112*, 109991. [\[CrossRef\]](#)
9. Zhang, J.; Zhang, M.; Li, Y.; Jiang, F.; Wu, L.; Guo, D. Comparison of wind characteristics in different directions of deep-cut gorges based on field measurements. *J. Wind Eng. Ind. Aerodyn.* **2021**, *212*, 104595. [\[CrossRef\]](#)
10. Ren, H.; Laima, S.; Chen, W.L.; Zhang, B.; Guo, A.; Li, H. Numerical simulation and prediction of spatial wind field under complex terrain. *J. Wind Eng. Ind. Aerodyn.* **2018**, *180*, 49–65. [\[CrossRef\]](#)
11. Li, X.; Gao, Y.; Pan, Y.; Xu, Y. Evaluation of near-surface wind speed simulations over the Tibetan Plateau from three dynamical downscalings based on WRF model. *Theor. Appl. Climatol.* **2018**, *134*, 1399–1411. [\[CrossRef\]](#)
12. Prieto-Herráez, D.; Frías-Paredes, L.; Cascón, J.M.; Lagüela-López, S.; Gastón-Romeo, M.; Asensio-Sevilla, M.I.; Martín-Nieto, I.; Fernandes-Correia, P.M.; Laiz-Alonso, P.; Carrasco-Díaz, O.F.; et al. Local wind speed forecasting based on WRF-HDWind coupling. *Atmos. Res.* **2021**, *248*, 105219. [\[CrossRef\]](#)
13. Xu, W.; Liu, P.; Cheng, L.; Zhou, Y.; Xia, Q.; Gong, Y.; Liu, Y. Multi-step wind speed prediction by combining a WRF simulation and an error correction strategy. *Renew. Energy* **2021**, *163*, 772–782. [\[CrossRef\]](#)
14. Zhang, Y.; Cao, S.; Zhao, L.; Cao, J. A case application of WRF-UCM models to the simulation of urban wind speed profiles in a typhoon. *J. Wind Eng. Ind. Aerodyn.* **2022**, *220*, 104874. [\[CrossRef\]](#)
15. Li, L.; Zhang, L.J.; Zhang, N.; Hu, F.; Jiang, Y.; Jiang, W.F. Application of FLUENT on the Fine-Scale Simulation of the Wind Field over Complex Terrain. *Plateau Meteorol.* **2010**, *29*, 621–628.
16. Song, J.L.; Li, J.W.; Xu, R.Z.; Flay, R.G. Field measurements and CFD simulations of wind characteristics at the Yellow River bridge site in a converging-channel terrain. *Eng. Appl. Comput. Fluid Mech.* **2022**, *16*, 58–72. [\[CrossRef\]](#)
17. Wang, K.; Liang, H.; Yan, Y. Wind field law of different terrain patterns based on computational fluid dynamics simulation and application in wind sensing planning. *Acta Ecol. Sin.* **2021**, *41*, 3499–3511. [\[CrossRef\]](#)
18. Zhuo, Z.L.; Li, Y.L.; Liao, H.L. Effect of ground surface roughness on wind field over bridge site with a gorge in mountainous area. *Eng. Mech.* **2017**, *34*, 73–81. [\[CrossRef\]](#)

19. Yang, Q.; Zhou, T.; Yan, B.; Liu, M.; Van Phuc, P.; Shu, Z. LES study of topographical effects of simplified 3D hills with different slopes on ABL flows considering terrain exposure conditions. *J. Wind Eng. Ind. Aerodyn.* **2021**, *210*, 104513. [[CrossRef](#)]
20. Chen, Z.; Wei, C.; Yin, L.; Su, N.; Zhao, J.; Wu, Y. Interference effects on the wind loads and wind-induced responses of parallel-arranged rectangular-planed air-supported membrane structures. *Thin-Walled Struct.* **2024**, *197*, 111572. [[CrossRef](#)]
21. Pal, S.; Raj, R.; Anbukumar, S. Comparative study of wind induced mutual interference effects on square and fish-plan shape tall buildings. *Sādhanā* **2021**, *46*, 86. [[CrossRef](#)]
22. Sharma, D.; Pal, S.; Raj, R. Effect of spacing on wind-induced interference on the roof of low-rise buildings with cylindrical roof using CFD simulation. *Sādhanā* **2023**, *48*, 283. [[CrossRef](#)]
23. Wu, K.; Wang, S.J.; Zhang, G.P.; Wie, M.; Liu, F.S.; Lu, X. Wind-induced interference effects and wind pressure characteristics of arched plastic greenhouses. *Trans. Chin. Soc. Agric. Eng. (Trans. CSAE)* **2019**, *35*, 165–174. [[CrossRef](#)]
24. Ci, W.; Zhuo, M. Lhasa City Surface Layer Wind Environmental Characteristics of the Preliminary Analysis. *Clim. Chang. Res. Lett.* **2017**, *6*, 8–12. [[CrossRef](#)]
25. Li, C.; Zhou, S.; Xiao, Y.; Huang, Q.; Li, L.; Chan, P.W. Effects of inflow conditions on mountainous/urban wind environment simulation. *Build. Simul.* **2017**, *10*, 573–588. [[CrossRef](#)]
26. Hong, S.; Lee, I.; Hwang, H.; Seo, I.; Bitog, J.; Kwon, K.; Song, J.; Moon, O.; Kim, K.; Ko, H. CFD modelling of livestock odour dispersion over complex terrain, part I: Topographical modelling. *Biosyst. Eng.* **2011**, *108*, 253–264. [[CrossRef](#)]
27. Xing, L.W. Inversion of Multi-Temporal Chinese Land Surface Vegetation Aerodynamic Roughness Based on MODIS and GLAS Data. Master's Thesis, Capital Normal University, Beijing, China, 2012.
28. Liu, X.P.; Dong, Z.B. Reviews of aerodynamic roughness length. *J. Desert Res.* **2003**, *23*, 337–346.
29. Stangroom, P. CFD Modelling of Wind Flow over Terrain. Ph.D. Thesis, Cranfield University, Cranfield, UK, 2004.
30. Guo, X.J. Study on Thermal Performance of Heating Radiators in High Altitude Cold Regions. Master's Thesis, Chongqing University, Chongqing, China, 2014.
31. *China Code GB 50009-2012*; Load Code for the Design of Building Structures. China Building Industry Press: Beijing, China, 2012.
32. Li, Q.Z.; Liu, N.H.; Huang, D.L. Calculation and practical application of gravitational acceleration values. *Meas. Tech.* **2001**, *4*, 11–15. [[CrossRef](#)]
33. Pattanapol, W.; Wakes, S.J.; Hilton, M.J.; Dickinson, K.J. Modeling of surface roughness for flow over a complex vegetated surface. *Int. J. Environ. Ecol. Eng.* **2007**, *1*, 94–102. [[CrossRef](#)]
34. Blocken, B.; Stathopoulos, T.; Carmeliet, J. CFD simulation of the atmospheric boundary layer: Wall function problems. *Atmos. Environ.* **2007**, *41*, 238–252. [[CrossRef](#)]
35. *China Code GB/T 51183-2016*; Code for the Design Load of Horticultural Greenhouse Structures. China Planning Press: Beijing, China, 2016.
36. Yan, W.H.; Wang, C.J.; Wu, D.H.; Huang, Z. Research on wind-induced interference effects in folding camping tent groups. *Eng. Mech.* **2016**, *33*, 166–175. [[CrossRef](#)]

**Disclaimer/Publisher's Note:** The statements, opinions and data contained in all publications are solely those of the individual author(s) and contributor(s) and not of MDPI and/or the editor(s). MDPI and/or the editor(s) disclaim responsibility for any injury to people or property resulting from any ideas, methods, instructions or products referred to in the content.